

Large-Eddy Simulation of the Convective Boundary Layer: A Comparison of Four Computer Codes

F.T.M. Nieuwstadt¹, P.J. Mason², C-H. Moeng³ and U. Schumann⁴

¹ Laboratory of Aero and Hydrodynamics, Delft University of Technology, 2628 AL Delft, The Netherlands

² Meteorological Office, Bracknell, Berkshire RG12 2SZ, England

³ National Center for Atmospheric Research, Boulder, CO 80307, USA

⁴ DLR, Institute of Atmospheric Physics, W-8031 Oberpfaffenhofen, Germany

Abstract

To test the consistency of large-eddy simulation we have run four existing large-eddy codes for the same case of the convective atmospheric boundary layer. The four models differ in various details, such as: the subgrid model, numerics and boundary conditions.

The agreement between the four models is excellent. In general model results lie within the scatter of available observations. Most of the disagreement between the model results can be attributed to the parameter C_s of the subgrid model. The effect of other differences between the four models, such e.g. due to numerics, is found to be small.

1. Introduction

In large-eddy simulation we seek to compute the large scales of turbulence. This is accomplished by performing on the Navier-Stokes equations a filter operation, designed to remove the small scales from these equations. The resulting set of equations is then solved numerically. Large-eddy simulation is considered to be a tool to study the details of turbulence and it is enjoying an increasing popularity.

The most successful application of large-eddy modelling has been to the atmospheric boundary layer and in particular the convective boundary layer. The reason is of course that the convective boundary layer is dominated by large structures. These are known as thermals and they are responsible for most of the vertical transport processes. They make the convective boundary layer an ideal subject for large-eddy simulation.

The study of the convective boundary layer with large-eddy models has started with the pioneering work of Deardorff in the seventies (e.g. Deardorff 1974). Since then extensive and detailed simulations have been reported by Moeng (1984), Mason (1989) and Schmidt & Schumann (1989). A more general review of large-eddy simulation of convection is presented by Nieuwstadt (1990)

Here, we will not add another simulation to this list. Instead this study has a different objective.

The philosophy of large-eddy modelling is to isolate the dynamics of the large scales. The small scales are treated by a more or less simple parameterization: the so-called subgrid model. This approach hinges on the hypothesis that the actual details of the subgrid model have only minor effects on the large scales. As this may be considered the fundamental premise of large-eddy modelling there are also other uncertainties. Any large-eddy model requires a large number of assumptions about details of the model, ranging from the choice of a numerical scheme to the selection of boundary conditions. It would be very undesirable if a large-eddy simulation turns out to be sensitive to these modelling details.

In this paper we aim to address these questions and investigate whether present large-eddy models are in line with the philosophy mentioned above. Do they lead to consistent simulations for the case of the convective atmospheric boundary layer? Such consistency would present a further argument that large-eddy simulations can be trusted to give a realistic representation of atmospheric turbulence.

To this end four research groups represented by the authors of this paper have decided to test their large-eddy models for a simulation of the convective boundary layer. Besides using different subgrid models, these codes also differ in many other details. We run the models starting from the same initial conditions and using the same forcing. By comparing the results we expect to learn the sensitivity of these models to the various parameters.

First we shall discuss in some detail the differences between the models. Next we shall specify the initial conditions and the calculation procedure. Then we turn to a discussion of the results. In particular we will consider in some detail the effect of the subgrid model.

2. Description of Large-Eddy Codes

As already mentioned above we shall use in this study existing large-eddy codes which have already been described elsewhere (Mason, 1989; Moeng, 1984; Nieuwstadt & Brost, 1986 and Schmidt & Schumann, 1989). Therefore, we shall restrict ourselves in this section to highlighting the various differences between the four models.

2.1 Subgrid Model

The main purpose of a subgrid model is to "dissipate" the energy which is passed down the cascade from the large eddies. Views at present differ on the complexity needed to model the subgrid terms.

The most simple parameterization is the well-known Smagorinsky model, which relates the subgrid stresses to the deformation of the resolved velocity field by means of an eddy viscosity, K_M . This eddy viscosity is expressed as

$$K_M = \ell^2 S \quad (1)$$

where S is the absolute value of the strain rate and ℓ is the so-called mixing length. This mixing length is proportional to the filter length.

The Smagorinsky model is used by Mason and for a more detailed discussion we refer to Mason & Callen (1986) and Mason (1989). In particular Mason (1989) introduces an extension of (1) to convective turbulence. Here, it suffices to mention that in the context of the Smagorinsky model a fundamental role is played by the coefficient C_s . It is defined as the ratio between the mixing length and a characteristic grid size Δ

$$C_s = \ell / \Delta. \quad (2)$$

Mason (1989) has considered the effect of several values for C_s and recommends $C_s = 0.32$.

Alongside the Smagorinsky model for subgrid stresses, an analogous model is used to parameterize subgrid heat fluxes. It relates the temperature flux to the resolved temperature gradient by means of an eddy diffusivity K_H . The K_H is connected to the K_M by means of a turbulent Prandtl number

$$Pr = \frac{K_M}{K_H}. \quad (3)$$

A slightly more complicated subgrid closure model is used by Moeng and Nieuwstadt. It is also based on a relation between the subgrid stress and the resolved deformation rate but in this case the eddy viscosity is defined as

$$K_M = 0.12 \Delta e^{1/2} \quad (4)$$

where e is the subgrid energy. A separate equation for the subgrid energy is formulated, which is then solved along with the other equations of the large-eddy model (Moeng, 1984). If we simplify the subgrid energy equation to a balance between shear production and dissipation, we may derive a representative value for C_s . In case of the subgrid model of both Moeng and Nieuwstadt, we find $C_s = 0.18$.

Schumann adopts the most complicated subgrid model. It is a second order closure model, in which the following simplifications are made. Only for the subgrid energy a full equation, including time derivatives and transport terms, is solved. In the other equations of the subgrid model these terms are neglected. Moreover, the production terms in these equations are limited to the isotropic part. As a result the subgrid model can be expressed as a decoupled algebraic system of equations, which can be explicitly solved. For further details we refer to Schmidt and Schumann (1989), where it is also derived that their representative value for C_s is: $C_s = 0.165$.

Another detail of the subgrid models which varies between the four codes is the formulation of the mixing length. In the interior of the boundary layer all four authors take the mixing length ℓ proportional to a characteristic grid size Δ . Moeng and Nieuwstadt use the geometric mean $\Delta = (\Delta x \Delta y \Delta z)^{1/3}$, whereas Schumann takes the arithmetic average: $\Delta = (\Delta x + \Delta y + \Delta z)/3$. Mason uses a non-uniform grid and he provides no explicit expression of Δ in terms of the grid spacing.

Furthermore, Mason and Schumann allow ℓ to become proportional to height when the surface is approached. Nieuwstadt takes this effect into account through a different parameterization of the dissipation term in the equation for e near the surface.

Finally, Mason, Moeng and Nieuwstadt limit the mixing length to a smaller value in stable conditions. This plays for instance a role in the stable layer above the boundary layer (Schumann, 1991).

Nevertheless, we shall see that the most important parameter influencing the effect of the subgrid model is C_s and perhaps to a lesser extent the Prandtl number Pr . For convenience we have collected these parameters in table 1.

Table 1. Representative values of the coefficient C_s and the turbulent Prandtl number Pr for the subgrid model of the four large-eddy codes.

	Mason	Moeng	Nieuwstadt	Schumann
C_s	0.32	0.18	0.18	0.165
Pr	0.46	0.33	0.33	0.42

2.2 Numerics

The models of Mason, Nieuwstadt and Schumann use a full staggered grid. This means that the velocity components are defined on the sides of the rectangular grid volume with the pressure in the centre. Moeng uses staggering only in the vertical direction, so that in her model all variables are defined on the same x, y -position.

The subgrid energy ϵ , used in the subgrid models of Nieuwstadt and Schumann is also defined in the centre of the grid volume. This means that in these models the exchange coefficients are located on the same position. Mason and Moeng adopt a different view and collocate the exchange coefficients with the w -point to avoid vertical averaging of z -derivatives.

The resolved temperature is governed by an advection-diffusion equation. Therefore, the most obvious location for the temperature is the centre of the grid volume. This view is taken by all participants except Nieuwstadt, who stores the temperature at the w -point. His argument is to avoid vertical averaging of temperature in the w -equation, where buoyancy is the dominant forcing term.

Next we consider the numerical schemes. With respect to time advancement Moeng and Schumann use the Adams-Bashford scheme, whereas Mason and Nieuwstadt employ the leap-frog method. The leap-frog scheme is unstable for the diffusion terms. Therefore, the latter authors resort for these terms to the simple forward Euler scheme.

Mason and Nieuwstadt treat the advection terms by scheme proposed by Piascek and Williams (1970). This is a second-order method designed to conserve variances even if the continuity equation is satisfied only approximately. Schumann uses standard second-order differencing for the momentum equations which conserves kinetic energy if the continuity equation is satisfied. For the temperature, he uses a second-order upwind scheme which preserves positivity. All three authors take second-order, central differencing to solve the diffusion terms. Moeng adopts a somewhat different approach. She uses a pseudo-spectral method to calculate all horizontal derivatives and a finite difference technique to calculate the vertical derivative. To avoid aliasing errors in the pseudo-spectral technique all Fourier expansions are truncated beyond the wave number $2/3 k_{max}$.

All four authors use a mixed fast-Fourier and finite difference technique to solve the Poisson equation for the pressure.

2.3 Boundary Conditions

In all four models horizontal boundary conditions satisfy periodicity. However, differences are found in the specification of the vertical boundary conditions.

At the lower boundary the vertical velocity w is set equal to zero. For the horizontal velocities one resorts to Monin-Obukhov similarity. This means that a relation is specified between the surface stress and the horizontal velocity in the first grid cell. Furthermore, it is assumed that the velocity and stress are parallel.

The models of Mason, Moeng and Schumann specify the temperature flux at the surface. Surface similarity is then used to obtain the surface temperature T_s (i.e. the temperature at $z = z_0$) from the temperature calculated in the centre of the first grid volume. Nieuwstadt has to adopt a different procedure, because he defines the temperature at the location of the w -variable. He then uses surface-layer similarity to specify a relationship between the surface-temperature flux and the temperature difference across the first grid cell. Note that in convective conditions the temperature profile near the surface is strongly curved. This curvature cannot be resolved within the first grid cell. As a result the subgrid exchange coefficients in Nieuwstadt's model are revised in relation to the standard surface-layer expressions.

With respect to the upper boundary conditions all four models agree on stress free conditions: i.e. $\partial u / \partial z = \partial v / \partial z = 0$. Furthermore the temperature gradient at the top of the calculation domain is set equal to the gradient Γ , which is prescribed in the initial conditions as the temperature gradient above the boundary layer.

There are however, some important differences in the treatment of the vertical velocity at the upper boundary. The goal is to avoid reflecting gravity waves from the top of the model. Moeng and Schumann prescribe a radiation boundary condition which allows gravity waves to propagate out of the calculation domain. Mason uses an expanding grid near the top of the calculation domain in conjunction with a damping layer. Nieuwstadt also uses a damping layer but no expanding grid. The role of the damping layer is to dissipate gravity waves before they can reflect back into the boundary layer. This is accomplished by adding to the equations of motion in the upper part of the calculation domain a relaxation term. This relaxation term then damps fluctuations at a prescribed relaxation time scale. Nieuwstadt takes the relaxation time scale equal to 50 s at the highest calculation level. The relaxation time scale in his model is then increased by a factor of 5 at each computation level for the next 9 levels down.

3. Calculation

The calculations are performed in a rectangular domain. Its horizontal dimensions are $6400 \times 6400 \text{ m}^2$. The vertical domain size is 2400 m for the computations of Moeng, Nieuwstadt and Schumann and 8000 m for the computation of Mason (remember that the latter author uses a non-uniform, expanding grid in the upper part of the calculation domain).

To limit the computational effort for this comparison study we took only a modest number of grid points. All authors use 40 grid points for both horizontal directions.

This implies a horizontal grid spacing of $\Delta x = \Delta y = 160$ m. In the vertical direction Nieuwstadt and Schumann use also 40 grid points so in their case $\Delta z = 60$ m. Moeng takes 48 grid points which implies $\Delta z = 50$ m. As mentioned before Mason specifies a non-uniform grid with 68 grid points. Near the surface his grid spacing is $\Delta z = 20$ m and within the boundary layer a typical grid spacing amounts to $\Delta z = 80$ m. Near the top of the boundary layer the grid spacing is again reduced to about $\Delta z = 30$ m. The grid then expands to $\Delta z = 250$ m towards the top of the calculation domain.

Convection is driven by a constant temperature flux at the surface of $Q_s = \langle w'T' \rangle_0 = 0.06 \text{ K m s}^{-1}$. This flux is directly prescribed at the surface in the models of Mason, Moeng and Schumann. The model of Nieuwstadt requires a different procedure because the heat flux is not defined at the surface due to the w -location of the temperature variable. In his case a constant temperature increase was prescribed at the surface with a magnitude of $(dT/dt)_0 = 0.16 \text{ K hour}^{-1}$. With this value of $(dT/dt)_0$ the temperature flux varied slightly during the calculation, say between 0.061 K m s^{-1} and 0.058 K m s^{-1} . However, averaged over the whole calculation period the temperature flux was found to be equal to 0.06 K m s^{-1} .

The calculations were set up in such a way that boundary-layer height would reach a value in the neighbourhood of 1600 m. Therefore, we introduce as a scaling height $z_{i0} \equiv 1600$ m. We can now define a convective velocity scale w_{*0} as: $w_{*0} = [(g/T_0)Q_s z_{i0}]^{1/3}$. The gravitational acceleration g is taken here to be: $g = 9.81 \text{ m s}^{-2}$ and the reference temperature $T_0 = 300 \text{ K}$. A temperature scale can now be defined as $T_{*0} = Q_s/w_{*0}$ and a time scale as $t_* = z_{i0}/w_{*0}$. With the values of z_{i0} and Q_s mentioned above, w_{*0} becomes equal to 1.46 m s^{-1} , T_{*0} equal to 0.041 K and $t_* = 1096 \text{ s}$.

Note that in most presentations, to be discussed in the following section, we shall use instead w_* and T_* to scale the results. These variables are called the convective scales defined by

$$w_* = \left(\frac{g}{T_0} Q_s z_i\right)^{1/3}, \quad (5)$$

$$T_* = \frac{Q_s}{w_*},$$

where z_i is an actual boundary-layer height. That means a boundary-layer height representative for the time period for which the results are evaluated. This actual boundary layer height has in principle a different value for each calculation.

Other parameters of interest are the constant temperature gradient Γ above the boundary layer. This was specified to be $\Gamma = 0.003 \text{ K m}^{-1}$. Furthermore, the roughness length, which enters the surface similarity relationships, is taken to be $z_0 = 0.16$ m. The density ρ has been set to 1 kg m^{-3} because its value is irrelevant in the normalized results.

As initial conditions we prescribe the following profiles for the temperature T and the three velocity components u , v , w .

For $z < z_{i1} = 0.844 z_{i0}$

$$T = T_0 + 0.1r \left(1 - \frac{z}{z_{i1}}\right) T_{*0}$$

$$w = 0.1r \left(1 - \frac{z}{z_{i1}}\right) w_{*0}$$

$$u = v = 0$$

and for $z > z_{i1}$

$$T = T_0 + (z - z_{i1})\Gamma$$

$$u = v = w = 0.$$

In these equations r stands for a random number uniformly distributed between -0.5 and 0.5 .

In individual calculations these initial profiles are sometimes slightly modified. For instance, Nieuwstadt prescribes for the horizontal velocity components, u and v , at the lowest grid cell the value $0.01rw_{*0}$ to avoid problems with the surface-layer similarity relationships. Furthermore, he increases the temperature at the surface by 2 K with respect to the value specified by the profile above. Finally the subgrid energy is initialized in the models of Moeng, Nieuwstadt and Schumann with the profile proposed by Schmidt and Schumann (1989),

$$e = 0.1w_{*0}^2(1 - \frac{z}{z_{i0}}). \quad (6)$$

Starting from these initial profiles we ran our models with a constant forcing Q_s for a period of $10t_*$. It was expected that after this period turbulence would reach a quasi-stationary state. Next, calculations were continued for $10 < t/t_* < 11$. Within this time interval various quantities were calculated as averages over N_t timesteps. These are the quantities which we shall discuss in the following section. It also means that our results have been averaged over only one time-scale. As we shall see, this is too short to obtain stable statistics especially for the higher order moments.

Table 2. Several statistics of the computations; N_x, N_y, N_z : number of grid points in the two horizontal and the vertical directions; L_x, L_y, L_z : horizontal and vertical size of the computation domain; Δt : timestep; T_{CPU} : CPU time per time step; N_T : total number of time steps to calculate the time period $0 < t/t_* < 11$; N_t number of timesteps used in the calculation of averages.

	Mason	Moeng	Nieuwstadt	Schumann
N_x, N_y	40	40	40	40
N_z	68	48	40	40
L_x, L_y (m)	6400	6400	6400	6400
L_z (m)	8000	2400	2400	2400
Δt (s)	0.65	3	4.48	10.96
T_{CPU} (s)	23.55	1.15	0.86	1.33
Storage (M words)	0.64	0.53	1.75	2.3
Computer	IBM 3084	Cray-YMP	Cray-XMP	Cray-YMP
N_T	20000	4000	2750	1100
N_t	40	10	4	10

For further information we have summarized in table 2 various statistics of the four computations. Mason uses the smallest time step as required for stability in view of his small vertical grid spacing near the surface. Nieuwstadt's code performs most efficiently but the total computation time is smallest in Schumann's case because of the larger time step. The larger integration time per time step in Schumann's model is a consequence of the second-order upwind scheme for the temperature variable and the more complex

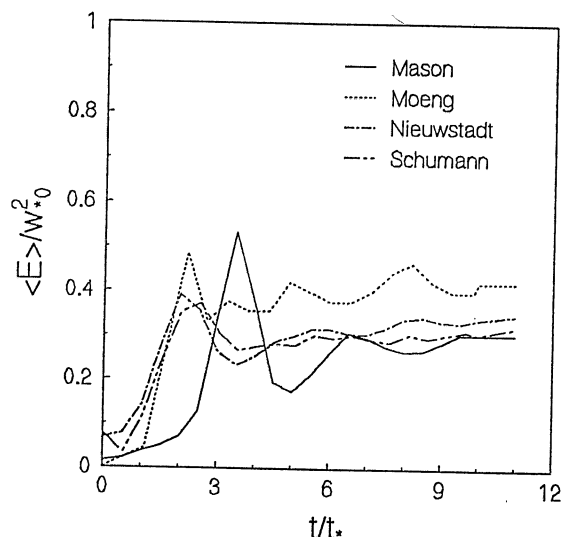


Fig. 1. The total kinetic energy vertically averaged across the boundary-layer height as a function of dimensionless time

subgrid model. His rather large storage requirements come from analysis parts which are executed during the integration. It is also interesting to note that the pseudo-spectral scheme of Moeng performs quite efficiently.

4. Results

First, we consider whether our simulations have indeed reached a state of quasi-stationary turbulence. To that end we have plotted in Fig. 1 the kinetic energy averaged across the boundary layer as a function of the dimensionless time t/t_* . Note that we have plotted the total energy $\langle E \rangle$ where $E = (u'^2 + v'^2 + w'^2)/2$, i.e. the resolved plus subgrid contribution $\langle e \rangle$. The energy quickly grows in the initial phase of the computation. After an overshoot it settles towards a constant value, which can be interpreted as reaching a state of quasi-stationary turbulence. The overshoot is presumably caused by initial development of large convective rolls, which at later time turn into more random motions. In the case of Mason's computation the overshoot occurs at a later time and it is also larger than for the other models. We believe this to be due to the larger value of C_s in Mason's subgrid model, which leads to a rapid initial loss of energy from the random perturbations. The fact that Moeng's results are somewhat larger than the other calculations seems to agree with her data for the variances to be presented later.

Another proof of quasi-stationarity is given in Fig. 2, where we show the profile of the temperature flux averaged over the time period $10 < t/t_* < 11$ as a function of dimensionless height. Quasi-stationarity should lead to a linear temperature flux profile in the boundary layer. This is very well satisfied by all models.

Fig. 2.

Tabel
temper
temper
are cal

z_i/z_t
w_*/v
$- <$
$T_s (K)$
$\bar{T} (K)$

Ar
peratu
by the
temper
averag

Th
subgri
flux ne
of usin

Ne
It resu
proces
the en

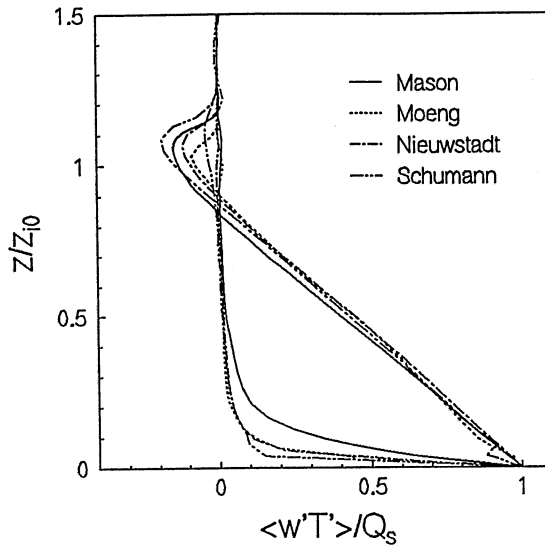


Fig. 2. The temperature flux profile as a function of dimensionless height z/z_{i0}

Table 3. The actual boundary-layer height z_i , the convective velocity scale w_* and the entrainment temperature flux $-\langle w'\theta' \rangle_i$ representative for the time period $10 < t/t_* < 11$; the surface temperature T_s ; the average boundary layer temperature above the surface layer \bar{T} (both T_s and \bar{T} are calculated at $t/t_* = 11$).

	Mason	Moeng	Nieuwstadt	Schumann
z_i/z_{i0}	1.0563	1.0312	1.0688	1.0900
w_*/w_{*0}	1.018	1.010	1.022	1.029
$-\langle w'\theta' \rangle_i / Q_s$	0.147	0.106	0.118	0.188
T_s (K)	302.17	301.53	302.54	302.5
\bar{T} (K)	300.55	300.57	300.58	300.57

Another well-known property of the convective boundary layer is that the mean temperature is approximately constant over most of the boundary layer. This is corroborated by the calculated temperature profiles (not shown). As additional information on the temperature profile we give in table 3 the value of the surface temperature T_s and the average boundary-layer temperature above the surface layer \bar{T} calculated at $t/t_* = 11$.

The contribution by the subgrid heat flux is small except near the surface, where subgrid effects should dominate by definition. The anomalous value of the temperature flux near the surface in Schumann's model should be disregarded because it is the result of using interpolations for statistics but upwind fluxes in the simulations.

Near the top of the turbulent boundary layer we observe a negative temperature flux. It results from the fact that the boundary layer grows into the stable layer above. This process is called entrainment. The minimum value of the temperature flux is defined as the entrainment flux, $-\langle w'\theta' \rangle_i$. Its value for the four models is given in table 3.

Note that the magnitude of this entrainment flux varies considerably between the four computations. As the entrainment flux is largely resolved, this must be a property of the individual models. However, we cannot offer at this stage an explanation of this behaviour in terms of the model parameters.

Furthermore we note that Schumann's model predicts the largest entrainment heat flux. This is partly due to the fact that his model calculates a considerable subgrid contribution to the entrainment flux. The explanation for this result lies in his formulation of the subgrid mixing length ℓ . Remember that Schumann's subgrid model uses a mixing length which is not limited by stability. Therefore it will lead to larger subgrid fluxes near the top of the boundary layer (Schumann, 1991).

The boundary-layer height z_i is defined as the height where the entrainment temperature flux occurs. Its value for the four models is entered in table 3. The height of the boundary-layer seems to correlate positively with the value of the entrainment flux. As already mentioned in the previous section we shall use this actual boundary-layer height to scale the calculation results of each model. In connection we will also use w_* , defined by (5). Its value is also entered in table .

4.1 Variances

In Fig. 3 we present the variance of the vertical velocity fluctuations as a function of z/z_i . We have plotted in this figure both the total variance, i.e. resolved plus subgrid, and the subgrid contribution.

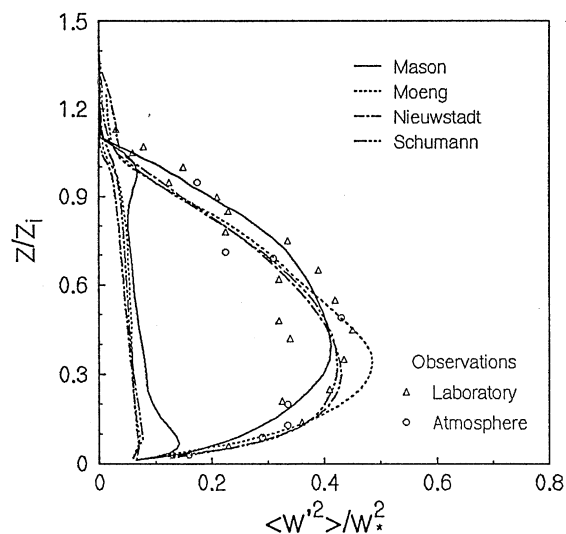


Fig. 3. The variance of vertical velocity fluctuation as a function of dimensionless height z/z_i ; plotted is the total variance (resolved plus subgrid) and the subgrid contribution; laboratory data are from Willis & Deardorff (1974) and Deardorff & Willis (1985); atmospheric data from Lenschow et al. (1980).

The subgrid model of Schumann allows a direct estimate of the subgrid contribution to $\langle w'^2 \rangle$. Moeng and Nieuwstadt calculate the subgrid energy e . They then assume isotropy so that for the subgrid contribution to $\langle w'^2 \rangle$ results $2/3e$. Mason estimates the subgrid energy from the following diagnostic relationship

$$e = a^{-2} \ell^2 S^2 (1 - Ri_f)$$

where Ri_f is the flux Richardson number equal to $Ri_f = g / (T_0 Pr) \partial T / \partial z / S^2$. The constant a is taken as 0.3. The contribution to $\langle w'^2 \rangle$ is then calculated by the same method as used by Moeng and Nieuwstadt.

The agreement between the four models is clearly excellent. Only Mason's model exhibits a slightly different profile. The other models only differ in their prediction of the maximum value of $\langle w'^2 \rangle$.

We have plotted in Fig. 3 also some observations obtained from laboratory experiments (Willis & Deardorff, 1974 and Deardorff & Willis, 1985) and from atmospheric field tests (Lenschow et al., 1980). Moreover, the present results agree closely with those of Schmidt & Schumann (1989) who used a much finer grid ($160 \times 160 \times 48$). It seems that the differences between the four models are smaller than the scatter in the experimental data. It is therefore not possible to conclude from this figure which model gives the best simulation. We will see that the same statement applies to other comparisons with observational data.

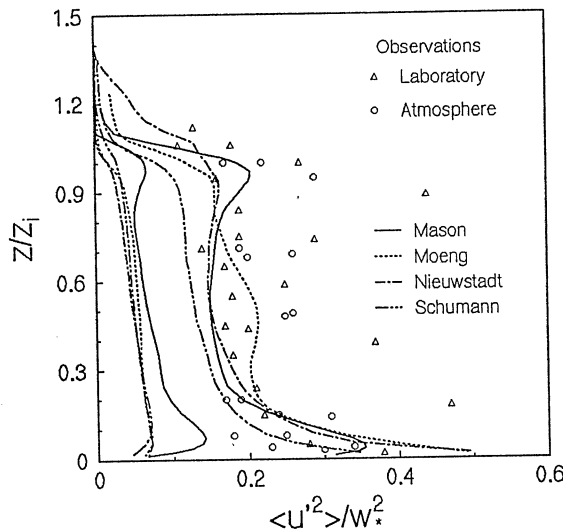


Fig. 4. The variance of horizontal velocity fluctuation as a function of dimensionless height z/z_i ; plotted is the total variance (resolved plus subgrid) and the subgrid contribution.

In Fig. 4 we show a dimensionless plot of the total horizontal velocity variance and its subgrid contribution. The subgrid contributions are calculated by the same method as discussed above for Fig. 3.

In this case differences between the four models are somewhat larger but they lie still within the scatter of the observations, also shown in this figure.

Points to be noted are: Mason's model shows a strong increase towards the top of the boundary layer. His results indicate dominance of large-scale thermals or rolls which span over the whole boundary-layer depth with strong horizontal components at the surface and near the inversion. In the next section we will find that this effect is due to the subgrid model. Moeng's profile exhibits a mid-layer maximum, which we believe to be unrealistic. It explains her somewhat larger values of the boundary-layer averaged energy found in Fig. 1. Finally, the results of Nieuwstadt show a large value of the variance near and even above the boundary-layer top. This is caused by his upper boundary condition, which uses a damping layer. It seems that the damping layer fails to remove fluctuations sufficiently.

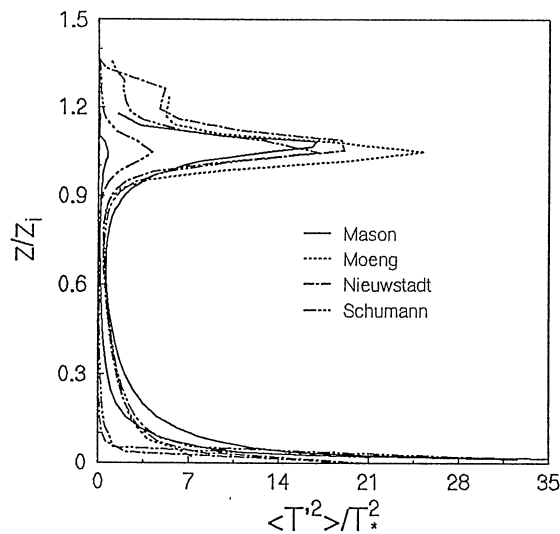


Fig. 5. The variance of temperature fluctuations as a function of dimensionless height z/z_i ; plotted is the total variance (resolved plus subgrid) and the subgrid contribution.

A dimensionless profile of the temperature variance is shown in Fig. 5. The subgrid contribution can be directly calculated by Schumann's model. Mason and Nieuwstadt estimate this contribution from

$$\langle T'^2 \rangle = a_T \frac{H^2}{e}$$

where H is the subgrid temperature flux. The value of the constant a_T is taken as 0.67.

The largest disagreement between the four models is found near the top of the boundary layer. This can be partly explained by differences in the temperature gradient. This gradient enters in the production term of the temperature variance and therefore determines the magnitude of $\langle T'^2 \rangle$. It turns out that Moeng's model, which has the largest variance, has indeed also the largest temperature gradient near the top of the boundary-layer. However, we should also mention here that she uses a somewhat different procedure to calculate her statistics compared with the other participants. Moeng scales her results at each calculation step with scaling variables appropriate for that time

step. After that she performs the average over the N_t time steps. The other authors average first their calculation results over the N_t time steps and then scale them with z_i and w_* representative for the whole averaging period. It is expected that the procedure of Moeng leads to somewhat higher variances.

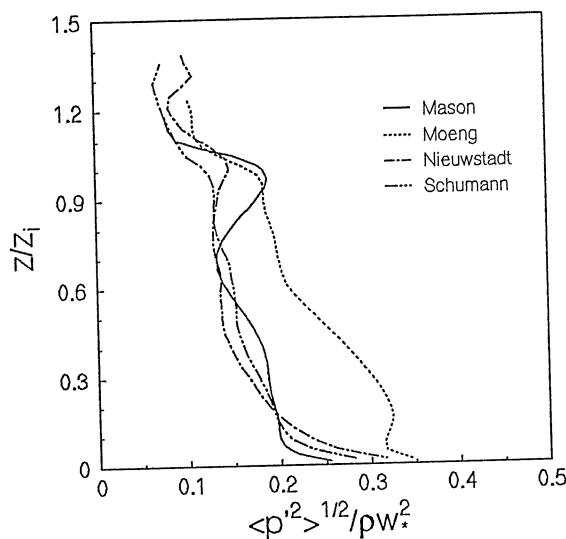


Fig. 6. The variance of pressure fluctuations as a function of dimensionless height z/z_i .

Finally, we give in Fig. 6 a dimensionless profile of the pressure variance. Except the data of Moeng all other models agree very well. An explanation for the deviating behaviour of Moeng's model cannot be offered.

Note that the pressure variance of Mason's model increases strongly towards the top of the boundary layer. The same behaviour was already found in Fig. 4 and we shall come back to it in the next section.

4.2 Higher Order Moments

In Fig. 7 we show the dimensionless profile of the third moment of the vertical velocity fluctuations. This variable is strongly influenced by the thermals in the convective boundary layer. A boundary layer consisting of isolated thermals with inside these a strong vertical upward motion, necessarily leads to a positive third moment as found in Fig. 7.

The agreement between the four models is quite acceptable in view of the observations which are also shown in the same figure.

The models of Moeng, Nieuwstadt and Schumann lead to a negative value of $\langle w'^3 \rangle$ near the surface. This is considered unrealistic because it would imply that downdrafts become stronger than updrafts when they approach the surface. Mason (1989) and Schmidt & Schumann (1989) have investigated the background of negative values of $\langle w'^3 \rangle$ in

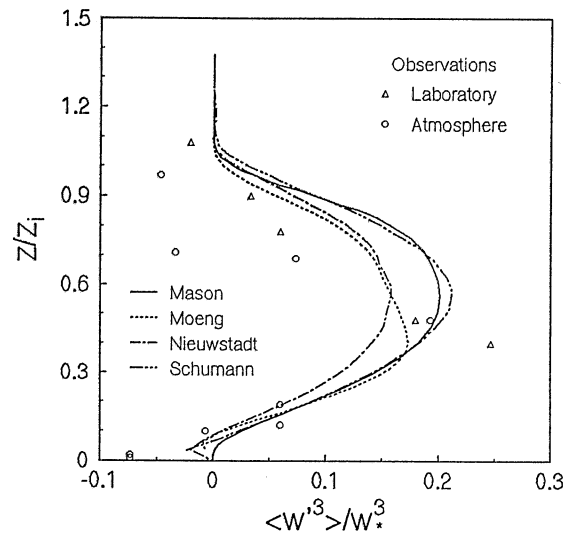


Fig. 7. The third moment of the vertical velocity fluctuations as a function of dimensionless height z/z_i .

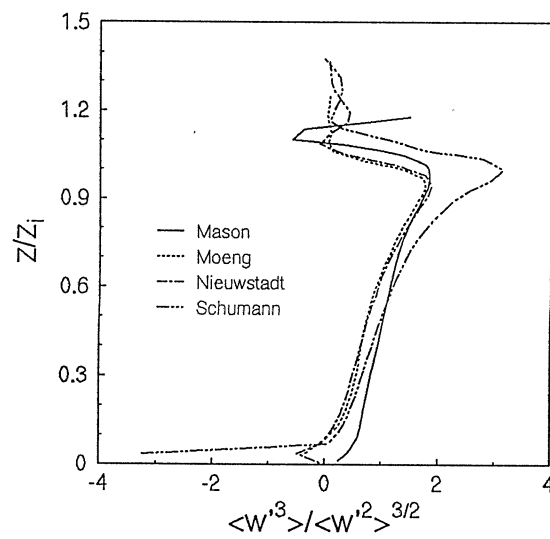


Fig. 8. The skewness Sk of the vertical velocity fluctuations as a function of dimensionless height z/z_i .

more detail. They conclude that it is a consequence of the subgrid model. Our calculations confirm this as we shall see in the next section.

The third moment can be combined with the variance to form a dimensionless parameter called skewness: $Sk = \langle w'^3 \rangle / \langle w'^2 \rangle^{3/2}$. Note that in this case both $\langle w'^2 \rangle$ and $\langle w'^3 \rangle$ are calculated from resolved motions only. The profile of Sk is shown in

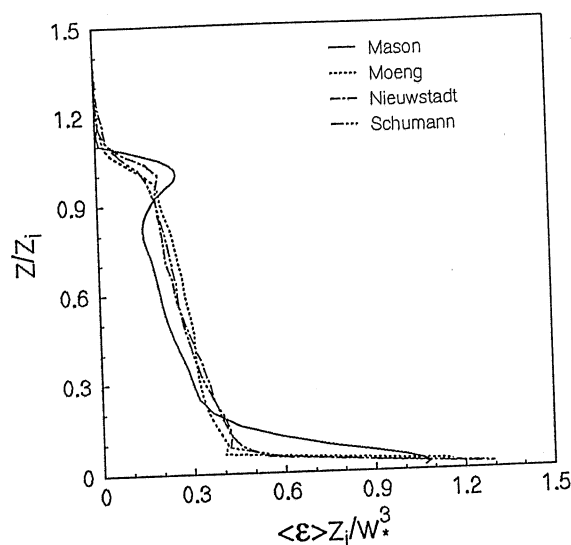


Fig. 9. The dissipation of turbulent kinetic energy as a function of dimensionless height z/z_i .

Fig. 8. The results of all models are again quite close. Schumann's data show a rather high value of Sk near the top of the boundary layer. This might be attributed to the fact that according to Fig. 7 his value of $\langle w'^3 \rangle$ is somewhat larger in this region compared with the other models. Nevertheless Fig. 7 also shows that this difference is rather small but its effect on Sk is magnified by the small values of $\langle w'^2 \rangle$ near the top of the boundary layer.

For a more detailed discussion of skewness in the convective boundary layer we refer to Moeng and Rotunno (1990). The comparison of the simulation results for Sk with observations is discussed by Lemone (1990).

4.3 Energy budget

The kinetic energy budget of turbulence in a quasi-stationary convective boundary layer reads

$$0 = \frac{g}{T_0} \langle w'\theta' \rangle - \frac{\partial}{\partial z} (\langle w'E' \rangle + \frac{1}{\rho} \langle p'w' \rangle) - \epsilon \quad (7)$$

where we have omitted the shear production term, which is zero in this case because $\langle u \rangle = 0$.

The first term in (7) denotes the production of kinetic energy by buoyancy forces. It is proportional to the temperature flux which we already have shown in Fig. 2. This production is balanced by the viscous dissipation ϵ which is computed from the subgrid model. Its vertical profile is given in Fig. 9. The agreement between the four models is excellent. Mason's calculation shows again a maximum towards the top of the boundary layer, the background of which will be disclosed in the next section. Moreover, we see

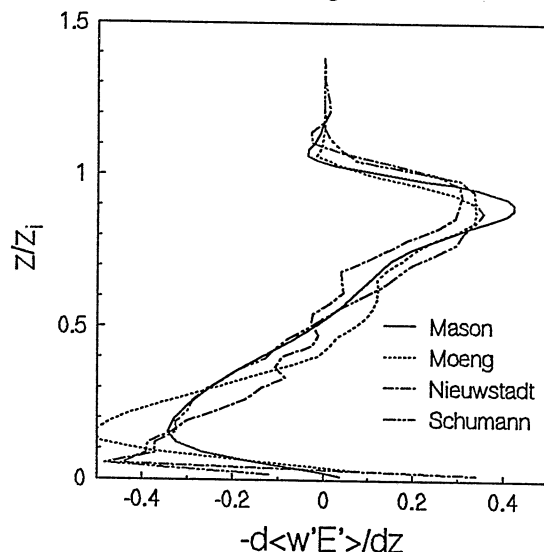


Fig. 10. The divergence of the vertical transport of kinetic energy (with as definition $E' = (u'^2 + v'^2 + w'^2)/2$) by velocity fluctuations, normalized by w_*^3/z_i , as a function of dimensionless height z/z_i .

that near the surface the ϵ calculated by the models of Moeng, Nieuwstadt and Schumann increase very rapidly. The model of Mason exhibits a more gradual profile. Schmidt & Schumann (1989) have pointed out that such rapid increase of ϵ usually goes together with a negative third moment near the surface as a dissipation excess requires downward transport of kinetic energy. This is indeed confirmed by our calculations and we remind the reader to the negative values of $\langle w^3 \rangle$ found in Fig. 7.

As the vertical profiles of the buoyancy production and dissipation are different we need the transport terms to satisfy the budget. The transport of kinetic energy by vertical velocity fluctuations, $\langle w'E' \rangle$, turns out to be the most important. Its profile is shown in Fig. 10. Despite some scatter, probably due to the inadequacy of averaging over only one time scale, the agreement between the four models seems again quite acceptable. However, this can no longer come as a surprise because we have already found good agreement for the production and the dissipation terms. The energy budget then forces agreement of the transport terms.

The profile of the pressure transport term $\langle p'w' \rangle$ is shown in Fig. 11. As suggested above its magnitude is indeed small. In view of this fact it is difficult to draw any conclusions from the rather large differences between the four models which we observe in Fig. 11. Moreover we note again that some of the scatter in Fig. 11 is probably again caused by the insufficient averaging period.

4.4 Conditional averages

In this subsection we discuss the properties of thermals by performing a conditional averaging procedure. It means that we calculate the average of a certain quantity only

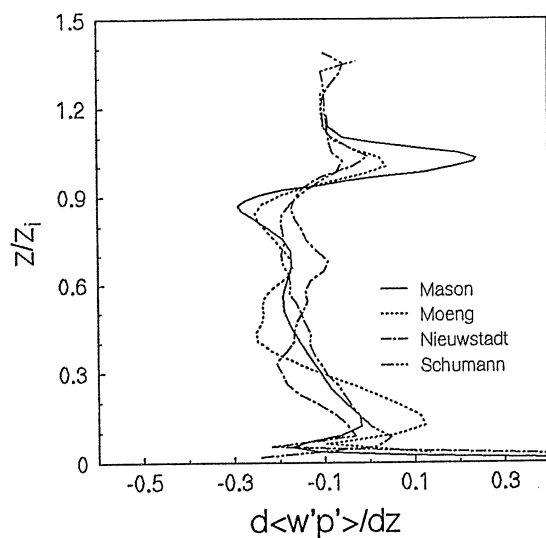


Fig. 11. The divergence of the vertical transport of kinetic energy by pressure fluctuations, normalized by $\rho w_*^3/z_i$, as a function of dimensionless height z/z_i .

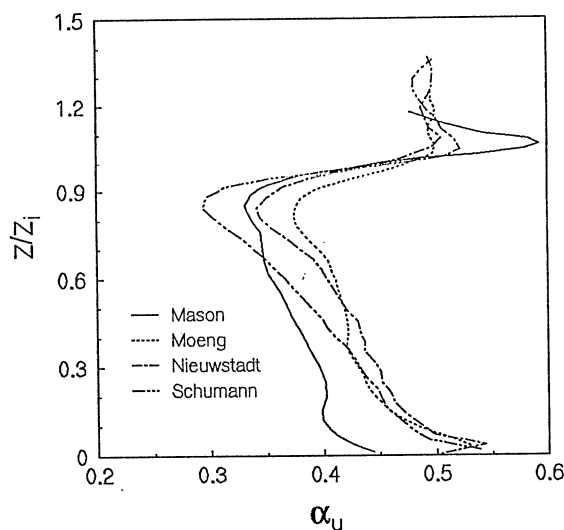


Fig. 12. The area fraction occupied by updrafts as a function of dimensionless height z/z_i .

over the area which is occupied by thermals, i.e. where $w > 0$. Let us first consider the area fraction α_u occupied by the thermals. It is shown in Fig. 12. It is interesting to note that this figure seems to be the mirror image of the skewness shown in Fig. 8.

In Figs. 13 and 14 we show the profiles of vertical velocity w_u and the mean temperature excess $T_u - \langle T \rangle$ in thermal areas characterized by $w > 0$. The agreement between the four models is surprisingly good.

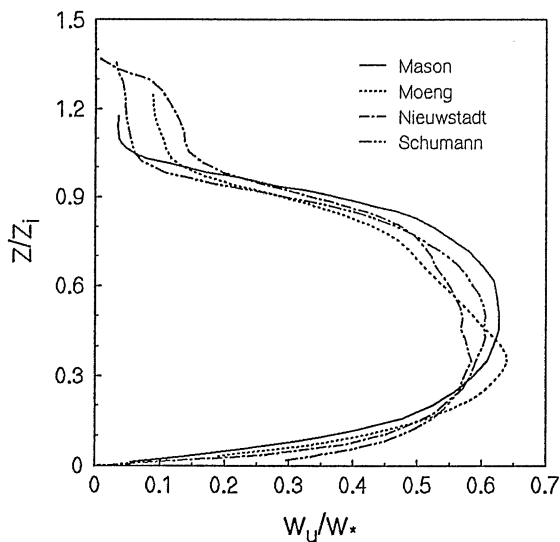


Fig. 13. The conditionally averaged vertical velocity in areas with $w > 0$ as a function of dimensionless height z/z_i .

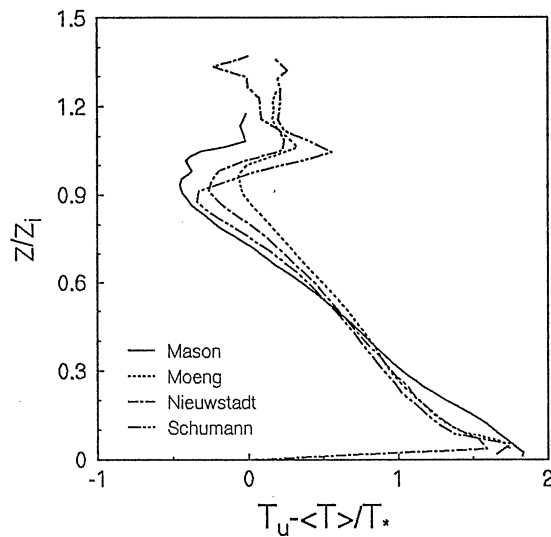


Fig. 14. The conditionally averaged temperature excess in areas with $w > 0$ as a function of dimensionless height z/z_i .

A point to note is the large value of w_u in Nieuwstadt's results above the boundary layer. This is again the consequence of his upper boundary condition.

For a more extensive discussion of conditional averages in the convective boundary layer we refer to Schumann and Moeng (1991a).

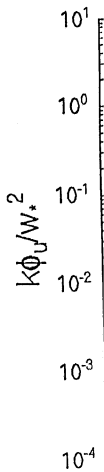


Fig. 15. T layer.

4.5 Spectral

In Figs. 13 and 14, the fluctuation spectra of the fluctuating vertical velocity and temperature excess are shown. The aliasing error is small ($kz_{i0} = 2$) for the values of kz_{i0} used.

One of the spectral calculations we shall discuss is the spectral calculation of the spectral density of the fluctuating vertical velocity.

However, the spectral calculation of the spectral density of the fluctuating vertical velocity is again very surprising. The spectral density of the fluctuating vertical velocity is shown in Fig. 15. The spectral density of the fluctuating vertical velocity is shown in Fig. 15. The spectral density of the fluctuating vertical velocity is shown in Fig. 15.

Finally, the spectral density of the fluctuating vertical velocity is shown in Fig. 15. The spectral density of the fluctuating vertical velocity is shown in Fig. 15. The spectral density of the fluctuating vertical velocity is shown in Fig. 15.

more r

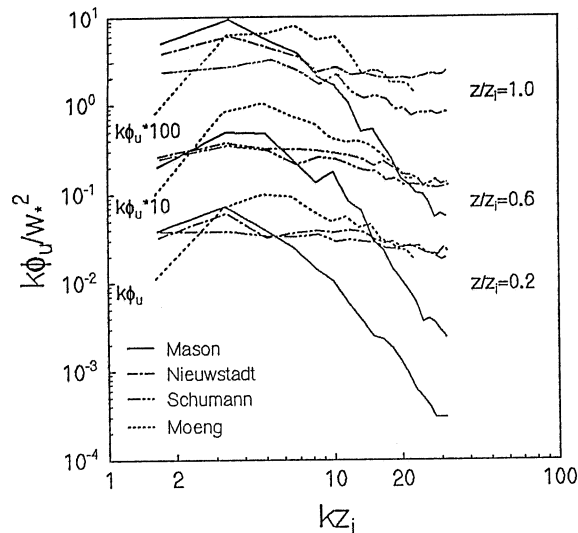


Fig. 15. The spectra of the resolved horizontal velocity fluctuations at three levels in the boundary layer.

4.5 Spectra

In Figs. 15 and 16 we show the spectra of the resolved horizontal and vertical velocity fluctuations at three levels in the boundary layer. The spectra of the resolved temperature fluctuations are given in Fig. 17. Remember that Moeng uses a spectral cut-off to avoid aliasing in her pseudo-spectral method. Therefore, her spectra stop beyond wave number $kz_{i0} = 22$ whereas the other spectra continue until $kz_{i0} = 29.84$ (in the figures the spectral values at the last wave number $kz_{i0} = 31.41$ have been omitted).

One fact which becomes immediately clear when we look at these figures is that the spectra of Mason have a much steeper slope at high wave numbers than the spectra calculated by the other models. This must clearly be an effect of the subgrid model and we shall come back to it in the next section.

However, we point to the fact that in all three figures the spectra of all models are again very close at low wave numbers, i.e. $kz_i \leq 10$. This should not come as a total surprise because it is consistent with the good agreement for the variances between all four models. Nevertheless, it supports the fundamental premise of large-eddy modelling, which we have stressed in our introduction: the large eddies do not depend strongly on the details of the subgrid model.

Finally, we should note that none of the spectra seems to follow the well-known $-2/3$ slope of the inertial range. However, this may be due to the rather poor resolution of our calculations, which is only 40^2 in the horizontal. There is some evidence (see e.g. Moeng and Wyngaard, 1988 and Schmidt and Schumann, 1989) that the spectra become more realistic at higher resolution.

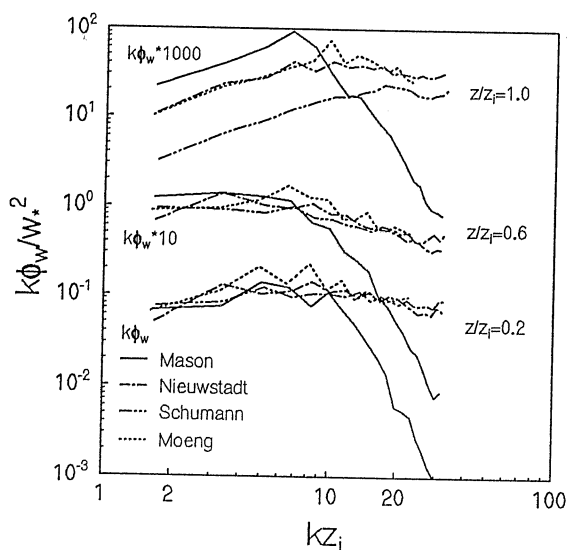


Fig. 16. The spectra of the resolved vertical velocity fluctuations at three levels in the boundary layer.

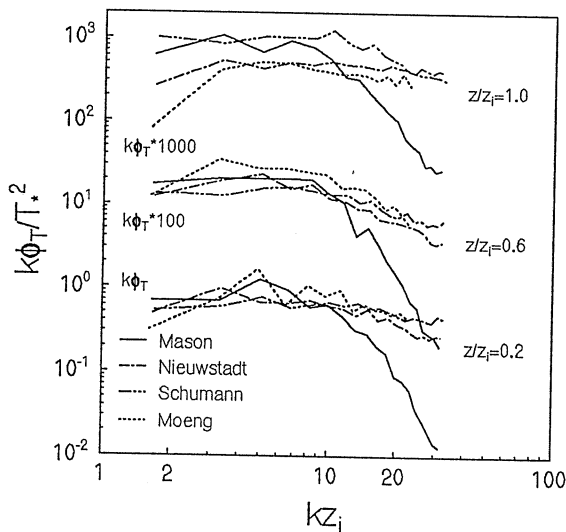


Fig. 17. The spectra of the resolved temperature fluctuations at three levels in the boundary layer.

5. Discussion

A main conclusion which we can draw from the results shown in the previous section is that the four models seem to fall into two categories with Mason in the one and Moeng,

Nieuwstadt and Schumann in the other. This distinction is shown in Fig. 17. In addition, the profile in con-

The main reason for this is the constant value of C_s whereas the value of C_s given in the literature with respect to the numbers is found to be different. This immediately

To test this, we have plotted the spectra of the resolved vertical velocity fluctuations at the same three levels in the boundary layer. At the same time, the equidistantly spaced profiles are primarily reflected in the same.

Let us compare the results with the following figure. The results are plotted in the same way as in the following figure.

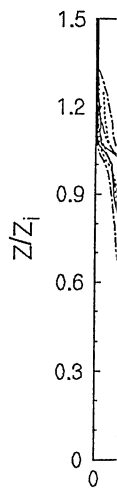


Fig. 18. The vertical profile of the resolved vertical velocity fluctuations at the same three levels in the boundary layer. The results are plotted in the same way as in the following figure.

First we compare the results with the following figure. The results are plotted in the same way as in the following figure.

Nieuwstadt and Schumann in the other. (However, in the latter group the models of Nieuwstadt and Schumann seem to agree slightly better). The most obvious support for this distinction into two groups is given by the results for the spectra shown in Figs. 15-17. In addition, Mason's model leads also frequently to a different shape of the vertical profile in comparison with results of the other models. Examples are Figs. 3, 4, 6 and 9.

The main difference in Mason's model with respect to the others is the values of the constant C_s . We have seen in table that for Mason's subgrid model $C_s = 0.32$, whereas the value of the other models vary around 0.18. According to the definition of C_s given in (2) this means that the mixing or filter length in Mason's model is larger with respect to the grid spacing. In other words, much of the variance at higher wave numbers is filtered out in comparison with the other models with smaller values of C_s . This immediately explains the behaviour of the spectra in Figs. 15-17.

To test this effect of C_s , Mason has rerun his model with a value of $C_s = 0.23$. At the same time he changed to an equidistant grid within the boundary layer with a representative vertical grid spacing of ~ 45 m. However, we expected that the effect of the equidistant versus non-uniform grid will be minimal. Therefore, the new results will primarily reflect the influence of C_s in Mason's model.

Let us consider a few of the results obtained from this additional calculation. They are plotted in the same format as used in the previous section. This means that in the following figures the results of Moeng, Nieuwstadt and Schumann have remained exactly the same.

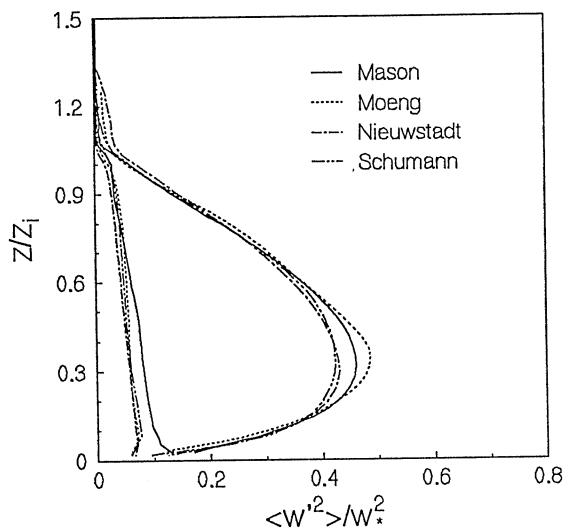


Fig. 18. The variance of vertical velocity fluctuation as a function of dimensionless height z/z_i ; plotted is the total variance (resolved plus subgrid) and the subgrid contribution. In comparison with Fig. 3 we have rerun Mason's model with $C_s = 0.23$ instead of $C_s = 0.32$. The results of Moeng, Nieuwstadt and Schumann have not been changed.

First we show the profile of the vertical variance in Fig. 18. If we compare this with Fig. 3 it is clear that the shape of Mason's profile has become much closer to the result

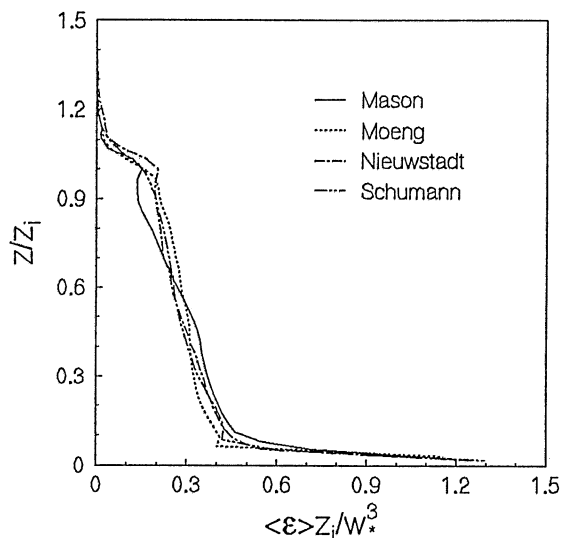


Fig. 19. The dissipation of turbulent kinetic energy as a function of dimensionless height z/z_i . In comparison with Fig. 9 we have rerun Mason's model with $C_s = 0.23$ instead of $C_s = 0.32$. The results of Moeng, Nieuwstadt and Schumann have not been changed.

of the other models. As a matter of fact the models are now almost indistinguishable and differ only in their prediction of the maximum value of $\langle w'^2 \rangle$.

Another effect which we consistently found in Mason's results presented in the previous section was a maximum in the profiles near the top of the boundary layer (see e.g. Figs. 4, 6, and 9). This phenomenon has completely disappeared for the new calculation. As an example we show in Fig. 19 the new results for the dissipation profile which we should compare with Fig. 9. The fact that the upper level maximum has disappeared may suggest that the large scale thermals in the new calculation have become somewhat weaker resulting in stronger small-scale motions. This suggestion is borne out by the results of the third moment $\langle w'^3 \rangle$, which for the new calculation are indeed found to be smaller.

Comparison of the Figs. 9 and 19 shows also that the behaviour of ϵ near the surface for the new results of Mason is now much closer to that of the other models. The rather gradual increase in ϵ , which we observed in Fig. 9, has disappeared and the ϵ increases now fast when the surface is approached. We have argued above that such a sudden increase of ϵ near the surface is consistent with a negative value of the third moment $\langle w'^3 \rangle$. Indeed, we find for Mason's new results that the $\langle w'^3 \rangle$ becomes negative at the lowest grid point.

Finally, we show in Fig. 20 the new spectra of the vertical velocity fluctuations. The agreement between the four models has much improved in comparison with Fig. 16, especially at the higher wave numbers. This result clearly confirms the effect of C_s . However, the slope of Mason's spectra in Fig. 20 is still somewhat steeper than that of the other models. This is consistent with the fact that $C_s = 0.23$ is still slightly larger than the representative C_s values of the other models.

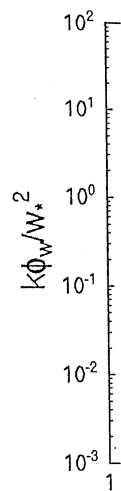


Fig. 20. The spectra of vertical velocity fluctuations. In comparison with Fig. 16, the agreement between the four models has much improved.

6. Conclusion

Our comparison leads to a number of conclusions. In many details the simulation results are in good agreement with the analytical models.

However, the convective case for large z/z_i is able to separate the convective and diffusive processes only 15 grid points above the surface. The same result is obtained in the modelling of the neutral case.

Based on the results of the models, the parameter of the parameter length and time scale at high wave numbers is large values. The vertical velocity fluctuations seem to be in good agreement with the modelling results.

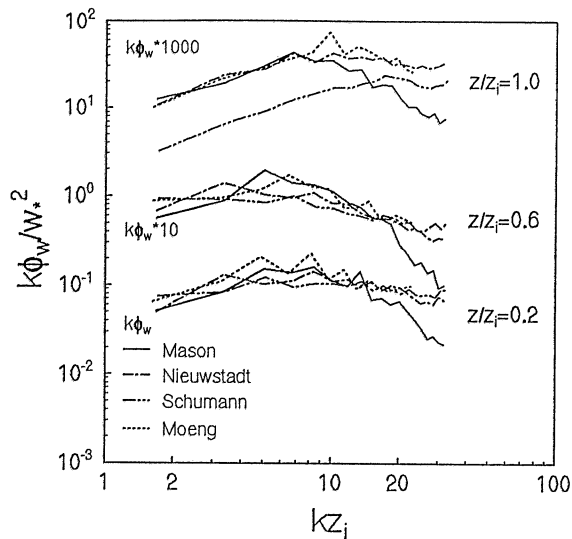


Fig. 20. The spectra of the resolved vertical velocity fluctuations at three levels in the boundary layer. In comparison with Fig. 16 we have rerun Mason's model with $C_s = 0.23$ instead of $C_s = 0.32$. The results of Moeng, Nieuwstadt and Schumann have not been changed.

6. Conclusion

Our comparison of four large-eddy codes has showed clearly that large-eddy simulation leads to a generally consistent picture of convective turbulence despite differences in many details of the models. This fact should strengthen our confidence in the realism of the simulated turbulence.

However, at this stage such statement can only be made for large-eddy simulation of convective turbulence. In other words, convective turbulence seems to be a rather easy case for large-eddy simulations. A relatively coarse resolution as used in this calculation is able to represent much of the salient characteristics of convective turbulence. In a separate calculation, Schumann (1991) found that an even coarser resolution, such as only 15 grid points distributed over the vertical domain of 2400 m, leads to about the same results. Shear turbulence seems to be more challenging test case for large-eddy modelling. Therefore, we are contemplating to perform a similar comparison study for the neutral boundary layer.

Based on this study we may draw several conclusions about details of our large-eddy models. The most important one concerns the subgrid model and in particular the value of the parameter C_s , which can be interpreted as the ratio between the mixing or filter length and the grid spacing. A large value of C_s leads to reduced values of the variance at high wave numbers in accordance with the notion of a larger filter length. Moreover, a large value of C_s results in somewhat stronger thermals at larger scales which influence the vertical profiles of some variables. Nevertheless, the effect of C_s on the large scales seems to be relatively minor, which supports the fundamental hypothesis of large-eddy modelling: the large eddies are little sensitive to the details of the subgrid model.

We have also found that the upper boundary condition should be formulated in such a way that gravity waves are not reflected from the top of the boundary layer. Otherwise we should expect to see increased values of the variance above the boundary layer. However, increased variances above the boundary layer do not seem to influence the simulation results inside the boundary layer. Nevertheless, we recommend the use of a radiation condition as upper boundary condition, which lets gravity waves propagate out of the domain. It seems to work very well and it is less expensive than an increase of the vertical computation domain together with an expanding grid.

Other differences between our four models which seem to have had hardly any effect on the calculation results, are: the numerical methods, the details of the staggered grid and the details of the lower boundary condition. For instance, there seems to be no advantage in applying a pseudo-spectral method (at least for a flow with small mean horizontal velocity). Also the use of a non-uniform versus an equidistant grid seems to have negligible influence. The only advantage of a non-uniform grid is perhaps that with a careful distribution of grid points one is perhaps able to get away with the use of fewer grid points.

Nevertheless, we should also point to what we believe to be genuine differences between the four models. These are differences, which can be attributed to the resolved scales. Examples are the entrainment temperature flux, the horizontal velocity fluctuations and perhaps also differences in the predicted maximum values of $\langle w'^2 \rangle$ and $\langle w'^3 \rangle$. The explanation for these admittedly rather small differences is not clear.

Acknowledgement

U. Schumann is grateful to Dr. Jutta Graf, who cooperated with him in this project. F.T.M. Nieuwstadt acknowledges discussions with J. Eggels and H. Cuypers and support from NWO-MFO project 752-365-022.

References

- Deardorff, J.W. 1974 Three dimensional numerical study of turbulence in an entraining mixed layer. *Boundary-Layer Met.* 7, 199-226
- Deardorff, J.W. & Willis, G.E. 1985 Further results from a laboratory model of the convective planetary boundary layer. *Boundary-Layer Met.* 32, 205-236
- Lemone, M. 1990 Some observations of vertical velocity skewness in the convective planetary boundary layer. *J. Atmos. Sci.* 47, 1163-1169
- Lenschow, D.H., Wyngaard, J.C. & Pennel, W.T. 1980 Mean-field and second-moment budgets in a baroclinic, convective boundary layer. *J. Atmos. Sci.* 37, 1313-1326
- Mason, P.J. 1989 Large-eddy simulation of the convective atmospheric boundary layer. *J. Atmos. Sci.* 46,
- Mason, P.J. & Callen N.S., 1986 On the magnitude of the subgrid-scale eddy coefficient in large eddy simulation of turbulent channel flow. *J. Fluid Mech.* 162, 439-462

- Moeng, C.-H. 1984 A large-eddy simulation for the study of planetary boundary layer turbulence. *J. Atmos. Sci.* **41**, 2052-2062
- Moeng, C.-H. & Rotunno, R. 1990 Vertical velocity skewness in the buoyancy driven boundary layer. *J. Atmos. Sci.* **47**, 1149-1162
- Moeng, C.-H. & Wyngaard, J.C. 1988 Spectral analysis of large-eddy simulations of the convective boundary layer. *J. Atmos. Sci.* **45**, 3574-3587.
- Nieuwstadt, F.T.M. 1990 Direct and large-eddy simulation of free convection. *Proc. 9th Internat. Heat Transfer Conference, Jerusalem 19-24 August 1990*, Amer. Soc. Mech. Engrg., New York, Vol I, 37-47
- Nieuwstadt, F.T.M. & Brost, R.A. 1986 Decay of convective turbulence. *J. Atmos. Sci.* **43**, 532-546
- Piascek S.A. & Williams, G.P. 1970 Conservation properties of convection difference schemes. *J. Comput. Phys.*, **6**, 392-405
- Schmidt, H. & Schumann, U. 1989 Coherent structures of the convective boundary layer derived from large-eddy simulations. *J. Fluid Mech.* **200**, 511-562
- Schumann, U. 1991 Subgrid length scales for large-eddy simulation of stratified turbulence. *Theor. Comput. Fluid Dynamics*, **2**, 279-290
- Schumann, U. & Moeng C.-H. 1991 Plume fluxes in clear and cloudy convective boundary layers. *J. Atmos. Sci.*, **48**, 1746-1757
- Willis, G.E. & Deardorff, J.W. 1974 A laboratory model of the unstable planetary boundary layer. *J. Atmos. Sci.* **31**, 1297-1307